Research Square

Preprints are preliminary reports that have not undergone peer review.
They should not be considered conclusive, used to inform clinical practice,
or referenced by the media as validated information.

Dynamics of telescopic boom crane with pulley-rope system based on movable nodes

Tianyu Wang
Dalian University of Technology
Zhaohui Qi
zhaohuiq@dlut.edu.cn
Dalian University of Technology
Tianjiao Zhao
Dalian University of Technology
Jinshuai Xu
Dalian University of Technology

Research Article

Keywords: multibody system dynamics, geometric nonlinearity beam, movable node, high-frequency oscillations

Posted Date: March 25th, 2026

DOI: https://doi.org/10.21203/rs.3.rs-9163425/v1

License: This work is licensed under a Creative Commons Attribution 4.0 International License.
Read Full License

Additional Declarations: No competing interests reported.

Version of Record: A version of this preprint was published at Multibody System Dynamics on July 16th, 2026. See the published version at https://doi.org/10.1007/s11044-026-10180-7.

Dynamics of telescopic boom crane with pulley-rope system based on movable nodes

Tianyu Wang, Zhaohui Qi, Tianjiao Zhao, Jinshuai Xu
School of Mechanics and Aerospace Engineering, Dalian University of Technology, Dalian, China, 116024, China

Abstract: Crane is a multibody system characterized by large displacements due to the coupling of its boom structure and pulley-rope system, both of which involve dynamic boundaries and dynamic loads. Since the boom undergoes significant deformation, conventional beam elements derived under the assumption of small deformations and rotations are not applicable. Due to the dynamic contact between pulley and rope, describing motion using material description is complex and insufficiently accurate. In this paper, the generalized strains of geometric nonlinearity beam element are derived to formulate the dynamic equations of the boom. The spatial description is adopted to characterize the relative motion between booms and the interaction between pulleys and ropes, leading to the establishment of elements with movable node. A model smoothing method is applied to filter out high-frequency oscillatory components of the system, significantly enhancing computational efficiency. Dynamic analysis of the crane system using the proposed method yields results with reasonable accuracy, which can provide support for the dynamic analysis of crane systems in engineering applications.

keyword: multibody system dynamics; geometric nonlinearity beam; movable node; high-frequency oscillations

1 Introduction

In order to ensure the operational safety of large cranes, conducting statics and dynamics analyses is essential, which is particularly crucial in the context of widespread applications of unmanned and intelligent systems[1-4]. Crane is multibody system which consists of boom system and a set of pulley-rope system (PRS), therefore characterized by dynamic contact. Boom is a box-type beam structure composed of multiple telescopic sections connected via pin joints, while the PRS is a rigid-flexible coupling system composed of drum, pulleys, and ropes.

The dynamic analysis of the aforementioned multibody system presents the following challenges:

1.Due to its length being significantly greater than its cross-sectional dimensions, the boom belongs to the category of slender beam structures and exhibits pronounced nonlinear effects, and the assumption of small deformations and rotations cannot be applied when deriving its generalized strains.

2.The contact between pulleys and ropes is a dynamic process, as illustrated in Fig.1.

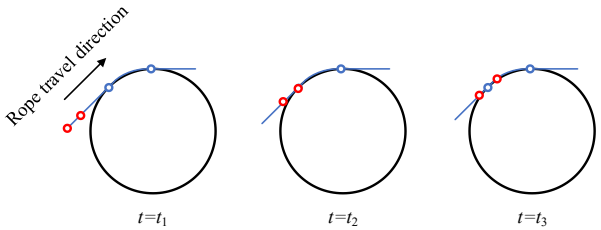


Fig.1 Dynamics contact of rope and pulley

The red points represent nodes constituting an element on the rope, which flow with the rope, and the blue points represent the contact nodes on the pulley. At time t_2 , the first node on rope comes into contact with the pulley, and subsequently enters it. At time t_3 , the node on pulley lies within the rope element. Traditional methods, such as the subdivision of cable elements, fail to address the issue where the contact point is located within a rope element. Moreover, ropes in different contact states exhibit varying shapes, a shape function which can accurately describe the geometry of both the straight-line segment and the arc segment of the cable cannot be created.

Researchers have studied large-deformation beam

elements via geometrically exact beam theory and ANCF. Combined with moving boundary and moving load issues, further studies are conducted[5-9]. Singh et al. combined geometrically exact kinematic description and robust finite element implementation, and simulated complex deployment scenarios involving spin, vibration, and length variation[10]. Sansour et al. developed an energy-momentum integration scheme for the geometrically exact Bernoulli-type rod, and studied its chaotic motions[11]. Tang et al. successfully demonstrated an ANCF-based variable-length tether element within a flexible multibody dynamics framework, which is used in satellite systems for space applications[12]. Sarvestan et al. presented a highly efficient and accurate SFEM-based framework for the vibration analysis of damaged viscoelastic structures under moving loads[13].

The pulley-rope system also constitutes a class of mechanical systems with flow-like characteristics, featuring moving boundaries. Ju established the finite element model of the rope using beam elements with reduced bending and torsion modulus, and conducted the static analysis of the pulley-rope system[14]. Chen et al. developed a two-dimensional dynamic model of the pulley and rope; however, while high-frequency vibration was observed in the result[15]. Peng et al. established the model of the pulley and the rope with ALE, attributing the tension difference across the two sides of the rope to friction[16]. Other researchers studied pulley-rope system in different lifting systems[17-23]. Commercial multibody software such as ADAMS typically employs a bushing force model to simulate pulley-rope systems, resulting in limited accuracy and an inability to capture detailed time-varying characteristics.

In this study, geometrical non-linear beam elements derived based on large deformation and rotation are employed, with the generalized strains defined as the axial strain and curvature of the beam cross-section. In order to address moving boundary problems, spatial description is adopted, and the contact points between ropes and pulleys are treated as movable nodes, and the material velocities and accelerations of the movable nodes are computed. Regarding high-frequency components in the system, model smoothing method presented in reference[24] is applied to lower the high-frequency of the generalized strains, while constraints are imposed on other quantities to mitigate their effects. To verify the correctness of the proposed method, several examples are conducted.

2 Element with movable nodes

2.1 Spatial description

In conventional finite element methods, the spatial distribution of nodes within the object remains unchanged, while the application of spatial description allows for the representation of changes in the positions occupied by movable nodes within the element. The origin of an arbitrary point can be expressed by both time and the material coordinate, which serves to define the position of a node within the object. A node whose material coordinates vary with time is termed a spatial point, in contrast to a material point. When describing complex motion of a mechanical system with moving boundary or moving loads, it would be more convenient to regard some crucial points as movable nodes.

As is shown in Fig.1, the blue points represent the contact points of the pulley and rope, which can be regarded as spatial points. The rope can be divided into segments in contact with the pulleys and segments between the pulleys by the contact points, thereby providing a more accurate description of the motion in a pulley-rope system.

The position vector of the contact point can be determined by time t and the original arc length s, which serves as the material coordinate. s changes with time, so one spatial point is occupied by different material points at different moments. The first and second order derivatives of the origin with respect to time has the following form based on the chain rule for differentiation.

$$\dot{\boldsymbol{r}}(t,s) = \frac{d\boldsymbol{r}}{dt} = \frac{\partial \boldsymbol{r}}{\partial t} + \frac{\partial \boldsymbol{r}}{\partial s}\dot{s} \tag{1}$$

$$\ddot{\boldsymbol{r}}(t,s) = \frac{d^2\boldsymbol{r}}{dt^2} = \frac{\partial^2 \boldsymbol{r}}{\partial t^2} + \frac{\partial \boldsymbol{r}}{\partial s}\ddot{s} + \frac{\partial^2 \boldsymbol{r}}{\partial s^2}\dot{s}^2 + 2\frac{\partial^2 \boldsymbol{r}}{\partial t \partial s}\dot{s} \tag{2}$$

According to eq.(1), $\partial \boldsymbol{r}/\partial t$ can be regarded as

the velocity of the material point whose material coordinate remains constant ($\dot{s}=0$). For spatial points, $\partial \boldsymbol{r}/\partial t$ is not equal to $d\boldsymbol{r}/dt$, because $\dot{s}\neq 0$. To distinguish the total time derivative d/dt and partial time derivative $\partial/\partial t$, the former is called spatial derivative and the latter is called material derivative in this paper, and the relationship between the two operators can be concluded as

$$\frac{\partial}{\partial t}=\frac{d}{dt}-\frac{\partial}{\partial s}\dot{s} \tag{3}$$

Similarly, according to eq.(2), the total and partial second order derivatives (d^2/dt^2 and $\partial^2/\partial t^2$) of the origin with respect to time is called spatial acceleration and material acceleration. For material points, spatial acceleration is equal to material acceleration, because the material coordinate remains constant, while for spatial points, spatial acceleration is not the same with material acceleration. The material and spatial acceleration can convert to each other, and the relationship can be written as

$$\frac{\partial^2}{\partial t^2}=\frac{d^2}{dt^2}-\frac{\partial}{\partial s}\ddot{s}-\frac{\partial^2}{\partial s^2}\dot{s}^2-2\frac{\partial^2}{\partial t\partial s}\dot{s} \tag{4}$$

In this paper, the symbols a' , a'' , a''' indicate the first to third derivatives of the variable with respect to the arc length, which have the form

$$a'\equiv\frac{\partial a}{\partial s},\ a''\equiv\frac{\partial^2 a}{\partial s^2},\ a'''\equiv\frac{\partial^3 a}{\partial s^3} \tag{5}$$

2.2 Principle of virtual power

The principle of virtual power is fundamental to establishing the static and dynamic equations of a complex mechanical system, which is an extension of Newton's laws of motion. The mass particle is the basic object in Newton's law of motion, so the virtual velocity in the principle of virtual power must be expressed in terms of material derivatives. The virtual power of a multibody system has the form

$$\begin{aligned}\delta w_f=&\int_0^L\delta(\frac{\partial\boldsymbol{\varepsilon}}{\partial t})^T\boldsymbol{\sigma}ds+\int_0^L\delta(\frac{\partial\boldsymbol{r}}{\partial t})^T\frac{\partial^2\boldsymbol{r}}{\partial t^2}\rho Ads\\&+\int_0^L\delta\boldsymbol{\omega}\cdot(\boldsymbol{J}\cdot(\frac{\partial\boldsymbol{\omega}}{\partial t})+\boldsymbol{\omega}\times\boldsymbol{J}\cdot\boldsymbol{\omega})\rho Ads\end{aligned} \tag{6}$$

In eq.(6), δw_f is the virtual power of the external force; s is the original arc length coordinate of arbitrary point on the centroid line of the beam, and $\boldsymbol{r}$ is its origin; $\boldsymbol{J}$ and A are the moment of inertia and area of the cross section; $\boldsymbol{\varepsilon}$ and $\boldsymbol{\sigma}$ are the generalized strain and stress; $\boldsymbol{\omega}$ is the material angular velocity of the cross section, which can be expressed under cardan description

$$\boldsymbol{\omega}=\boldsymbol{p}_1\frac{\partial\alpha}{\partial t}+\boldsymbol{p}_2\frac{\partial\beta}{\partial t}+\boldsymbol{p}_3\frac{\partial\gamma}{\partial t} \tag{7}$$

where, $\boldsymbol{p}_1,\boldsymbol{p}_2,\boldsymbol{p}_3$ are the rotation axes, and α,β,γ are the cardan angles correspondingly. Referring eq.(3), the material derivative of the generalized strain can be obtained

$$\frac{\partial\boldsymbol{\varepsilon}}{\partial t}=\dot{\boldsymbol{\varepsilon}}-\boldsymbol{\varepsilon}'\dot{s} \tag{8}$$

In order to establish the equation of a complex mechanical system according to the principle of virtual power, the following steps are required.

1. Select important connection points or joints, especially those with spatial point characteristics, and characterize the system motion.

2. Choose the individual describe variables as possible.

3. Compute each term in the equation of virtual power according to Eq.(6) and sum them up.

4. Handle the constraints if step 2 is not satisfied.

When forming the system of equations, material velocity and material acceleration are required if the node is spatial point. According to Eqs.(3)-(4), one can obtain material velocity and material acceleration from the change rate of the parameter.

3 Geometrical nonlinear beam element with moving nodes and the modeling of boom

The slenderness ratio of crane booms is typically on the order of tens to over a hundred, which often exhibit characteristics of large displacements and large rotations, necessitating the consideration of its geometric nonlinearity.

Telescopic boom cranes comprise multiple extendable booms assembled in a nested configuration, where adjacent booms are securely fastened together via pinned connections as Fig.2 shows. The mechanical fit between the current boom and its inner

boom is achieved through a pin joint, and the mechanical fit between the current boom and its outer boom is achieved through pin joint and the overlapping connection by the slider at the boom head.

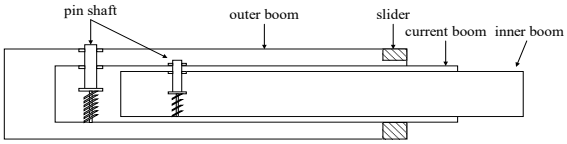


Fig.2 The interrelationships between the boom segments

Since the assumption of small displacement and rotation is abandoned, the force exerted by the slider on the boom is a moving load. Directly constraining the displacements and cardan angles of the related nodes of pin shafts and sliders can interfere with the deformation of the boom. Thus, the contact point with its outer boom on the current boom head should be modeled as a movable node.

3.1 Generalized strain of geometrical nonlinear beam element

According to the reference[25], when a beam element undergoes large deformations and rotations, the strains derived based on the assumptions of small displacements and small rotations are not applicable. In such cases, according to the principle of virtual power, the generalized strains of geometrically nonlinear beam elements are ε, the axial strain, and $(\kappa_s, \kappa_b, \kappa_t)$, the curvatures of the cross section. They can be obtained by the cardan angles of the cross section and the derivative of the origin of cross section's center with respect to arc length.

$$\varepsilon = \left\| \boldsymbol{r}_\xi' \right\| - 1 \tag{9}$$

$$\kappa_t = \beta' \sin\gamma + \alpha' \cos\beta \cos\gamma \tag{10}$$

$$\kappa_b = \beta' \cos\gamma - \alpha' \cos\beta \sin\gamma \tag{11}$$

$$\kappa_s = \alpha' \sin\beta + \gamma' \tag{12}$$

The constitutive relation can be expressed as

$$f_s = EA\varepsilon \tag{13}$$

$$m_t = EI_t\kappa_t \tag{14}$$

$$m_b = EI_b\kappa_b \tag{15}$$

$$m_s = GI_s\kappa_s \tag{16}$$

where, E is the elastic modulus, A is the area of the cross section, G is the shear modulus, and I_t, I_b, I_s are the moments of inertia of the cross section.

3.2 Application of movable nodes in boom modeling

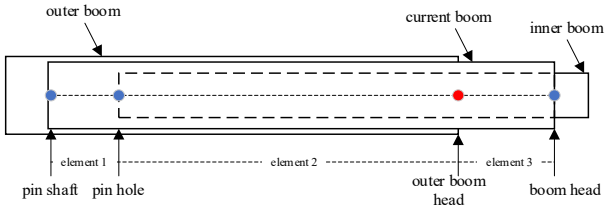


Fig.3 Discretization of boom element

For the current boom, the contact point with its outer boom at the boom head is designated as a movable node (red point in Fig.3). The current boom is divided into three beam elements by pin hole node and movable node. The nodal parameters of the current boom can be gathered as

$$\boldsymbol{q}_s = \left[\boldsymbol{r}_1; \cdots; \boldsymbol{r}_4; \frac{\partial \boldsymbol{r}_1}{\partial \xi}; \cdots; \frac{\partial \boldsymbol{r}_4}{\partial \xi}; \frac{\partial^2 \boldsymbol{r}_1}{\partial \xi^2}; \cdots; \frac{\partial^2 \boldsymbol{r}_4}{\partial \xi^2}; \gamma_1; \cdots; \gamma_4; s_{mov} \right] \tag{17}$$

where, the node numbered 1 is designated as the pin shaft node, and the node numbered 2 is designated as the pin hole node, and the node numbered 3 is designated as the outer boom head node (also the movable node), and the node numbered 4 is designated as the boom head node. s_{mov} is the arc length of the movable node. The origins of the nodes are $\boldsymbol{r}_i$, and their derivatives with respect to normalized coordinate ξ are $\partial \boldsymbol{r}_i / \partial \xi$ and $\partial^2 \boldsymbol{r}_i / \partial \xi^2$, and the first and second cardan angles can be solved from $\partial \boldsymbol{r}_i / \partial \xi$. γ_i, the third cardan angles, are the torsional angles of the nodes, and the arc length of the nodes are s_i.

Due to the requirement of curvature continuity, both displacements and cardan angles must be second-order continuous, necessitating the use of the fifth order Hermite interpolation. The origin of an arbitrary points in the element numbered i on the centroid line of the element can be approximated as

$$\boldsymbol{r}_\xi = N_1\boldsymbol{r}_i + N_2\boldsymbol{r}_{i+1} + N_3\boldsymbol{r}_i' + N_4\boldsymbol{r}_{i+1}' + N_5\boldsymbol{r}_i'' + N_6\boldsymbol{r}_{i+1}'' \triangleq \boldsymbol{N}\boldsymbol{v} \tag{18}$$

the shape functions are

$$N_1 = (1-\xi)^3(6\xi^2 + 3\xi + 1);\ N_2 = \xi^3(6\xi^2 - 15\xi + 10) \tag{19}$$

$$N_3 = \xi(1-\xi)^3(3\xi + 1)L;\ N_4 = \xi^3(7\xi - 3\xi^2 - 4)L \tag{20}$$

$$N_5 = \tfrac{1}{2}\xi^2(1-\xi)^3 L^2 \; ; \; N_6 = \tfrac{1}{2}\xi^3(1-\xi)^2 L^2 \tag{21}$$

The origins and their derivatives with respect to ξ , the normalized coordinates, are gathered as a column vector

$$\boldsymbol{v} = \left[\boldsymbol{r}_i; \boldsymbol{r}_{i+1}; \boldsymbol{r}_i'; \boldsymbol{r}_{i+1}'; \boldsymbol{r}_i''; \boldsymbol{r}_{i+1}''\right] \tag{22}$$

The shape functions are gathered as a row matrix as

$$\boldsymbol{N} = \left[N_1\boldsymbol{E}_{3\times3}, N_2\boldsymbol{E}_{3\times3}, N_3\boldsymbol{E}_{3\times3}, N_4\boldsymbol{E}_{3\times3}, N_5\boldsymbol{E}_{3\times3}, N_6\boldsymbol{E}_{3\times3}\right] \tag{23}$$

where, the length of the element

$$L = s_{i+1} - s_i \tag{24}$$

If an element contains moving nodes, the length of element will vary with time.

$$\dot{L} = \dot{s}_{i+1} - \dot{s}_i \tag{25}$$

Taking advantage of ξ , the change rate of the arc length of an arbitrary point can be written as

$$\dot{s} = \dot{s}_i + \xi\dot{L} \tag{26}$$

ξ should be regarded as constant when differentiating shape functions with respect to time. The spatial derivatives of shape functions can be expressed in the following form because they are functions of L .

$$\frac{\partial \boldsymbol{N}}{\partial t} = \dot{L}\frac{\partial \boldsymbol{N}}{\partial L} - \dot{s}\frac{\partial \boldsymbol{N}}{\partial s} \tag{27}$$

$$\frac{\partial^2 \boldsymbol{N}}{\partial t^2} = \ddot{L}\frac{\partial \boldsymbol{N}}{\partial L} - \ddot{s}\frac{\partial \boldsymbol{N}}{\partial s} + \dot{L}^2\frac{\partial^2 \boldsymbol{N}}{\partial L^2} - 2\dot{s}\dot{L}\frac{\partial \boldsymbol{N}}{\partial L}\frac{\partial \boldsymbol{N}}{\partial s} + \dot{s}^2\frac{\partial^2 \boldsymbol{N}}{\partial s^2} \tag{28}$$

By substituting Eqs.(25)-(26) into Eq.(27), the first-order material derivatives of the shape functions can be written as

$$\frac{\partial \boldsymbol{N}}{\partial t} = \boldsymbol{T}_{N_1}\dot{s}_i + \boldsymbol{T}_{N_2}\dot{s}_{i+1} \tag{29}$$

$$\frac{\partial \boldsymbol{N}'}{\partial t} = \boldsymbol{T}_{N_1'}\dot{s}_i + \boldsymbol{T}_{N_2'}\dot{s}_{i+1} \tag{30}$$

$$\frac{\partial \boldsymbol{N}''}{\partial t} = \boldsymbol{T}_{N_1''}\dot{s}_i + \boldsymbol{T}_{N_2''}\dot{s}_{i+1} \tag{31}$$

where, the transformation matrices

$$\boldsymbol{T}_{N_1} = -\frac{\partial \boldsymbol{N}}{\partial L} - \boldsymbol{N}'(1-\xi) \quad ; \quad \boldsymbol{T}_{N_2} = \frac{\partial \boldsymbol{N}}{\partial L} - \boldsymbol{N}'\xi \tag{32}$$

$$\boldsymbol{T}_{N_1'} = -\frac{\partial \boldsymbol{N}'}{\partial L} - \boldsymbol{N}''(1-\xi) \quad ; \quad \boldsymbol{T}_{N_2'} = \frac{\partial \boldsymbol{N}'}{\partial L} - \boldsymbol{N}''\xi \tag{33}$$

$$\boldsymbol{T}_{N_1''} = -\frac{\partial \boldsymbol{N}''}{\partial L} - \boldsymbol{N}'''(1-\xi) \quad ; \quad \boldsymbol{T}_{N_2''} = \frac{\partial \boldsymbol{N}''}{\partial L} - \boldsymbol{N}'''\xi \tag{34}$$

By substituting Eqs.(25)-(26) into Eq.(28), the second order material derivatives of the shape function can be obtained

$$\frac{\partial^2 \boldsymbol{N}}{\partial t^2} = \boldsymbol{T}_{N_1}\ddot{s}_i + \boldsymbol{T}_{N_2}\ddot{s}_{i+1} + \boldsymbol{\alpha}_N \tag{35}$$

$$\frac{\partial^2 \boldsymbol{N}'}{\partial t^2} = \boldsymbol{T}_{N_1'}\ddot{s}_i + \boldsymbol{T}_{N_2'}\ddot{s}_{i+1} + \boldsymbol{\alpha}_{N'} \tag{36}$$

$$\frac{\partial^2 \boldsymbol{N}''}{\partial t^2} = \boldsymbol{T}_{N_1''}\ddot{s}_i + \boldsymbol{T}_{N_2''}\ddot{s}_{i+1} + \boldsymbol{\alpha}_{N''} \tag{37}$$

where, the acceleration margins

$$\boldsymbol{\alpha}_N = \dot{L}^2\frac{\partial^2 N}{\partial L^2} + N''\dot{s}^2 - 2\frac{\partial N'}{\partial L}\dot{L}\dot{s} \tag{38}$$

$$\boldsymbol{\alpha}_{N'} = \dot{L}^2\frac{\partial^2 N'}{\partial L^2} + N'''\dot{s}^2 - 2\frac{\partial N''}{\partial L}\dot{L}\dot{s} \tag{39}$$

$$\boldsymbol{\alpha}_{N''} = \dot{L}^2\frac{\partial^2 N''}{\partial L^2} + N''''\dot{s}^2 - 2\frac{\partial N'''}{\partial L}\dot{L}\dot{s} \tag{40}$$

By substituting Eq.(27) and Eq.(29) into Eqs.(3), we can find that

$$\frac{\partial \boldsymbol{r}}{\partial t} = \boldsymbol{N}\dot{\boldsymbol{v}} + (\dot{s}_i\boldsymbol{T}_{N_1} + \dot{s}_{i+1}\boldsymbol{T}_{N_2})\boldsymbol{v} = \boldsymbol{T}_{r,q}\dot{\boldsymbol{q}}_s \tag{41}$$

$$\frac{\partial \boldsymbol{r}'}{\partial t} = \boldsymbol{N}'\dot{\boldsymbol{v}} + (\dot{s}_i\boldsymbol{T}_{N_1'} + \dot{s}_{i+1}\boldsymbol{T}_{N_2'})\boldsymbol{v} = \boldsymbol{T}_{r',q}\dot{\boldsymbol{q}}_s \tag{42}$$

$$\frac{\partial \boldsymbol{r}''}{\partial t} = \boldsymbol{N}''\dot{\boldsymbol{v}} + (\dot{s}_i\boldsymbol{T}_{N_1''} + \dot{s}_{i+1}\boldsymbol{T}_{N_2''})\boldsymbol{v} = \boldsymbol{T}_{r'',q}\dot{\boldsymbol{q}}_s \tag{43}$$

Similarly, the second order material derivatives of origin can be expressed as

$$\begin{aligned}\frac{\partial^2 \boldsymbol{r}}{\partial t^2} &= \boldsymbol{T}_{r,q}\ddot{\boldsymbol{q}}_s + \boldsymbol{\alpha}_{r,q} \\ &= \boldsymbol{N}\ddot{\boldsymbol{v}} + (\ddot{s}_i\boldsymbol{T}_{N_1} + \ddot{s}_{i+1}\boldsymbol{T}_{N_2} + \boldsymbol{\alpha}_N)\boldsymbol{v} + 2\frac{\partial \boldsymbol{N}}{\partial t}\dot{\boldsymbol{v}}\end{aligned} \tag{44}$$

$$\begin{aligned}\frac{\partial^2 \boldsymbol{r}'}{\partial t^2} &= \boldsymbol{T}_{r',q}\ddot{\boldsymbol{q}}_s + \boldsymbol{\alpha}_{r',q} \\ &= \boldsymbol{N}'\ddot{\boldsymbol{v}} + (\ddot{s}_i\boldsymbol{T}_{N_1'} + \ddot{s}_{i+1}\boldsymbol{T}_{N_2'} + \boldsymbol{\alpha}_{N'})\boldsymbol{v} + 2\frac{\partial \boldsymbol{N}'}{\partial t}\dot{\boldsymbol{v}}\end{aligned} \tag{45}$$

$$\begin{aligned}\frac{\partial^2 \boldsymbol{r}''}{\partial t^2} &= \boldsymbol{T}_{r'',q}\ddot{\boldsymbol{q}}_s + \boldsymbol{\alpha}_{r'',q} \\ &= \boldsymbol{N}''\ddot{\boldsymbol{v}} + (\ddot{s}_i\boldsymbol{T}_{N_1''} + \ddot{s}_{i+1}\boldsymbol{T}_{N_2''} + \boldsymbol{\alpha}_{N''})\boldsymbol{v} + 2\frac{\partial \boldsymbol{N}''}{\partial t}\dot{\boldsymbol{v}}\end{aligned} \tag{46}$$

The material derivatives of the generalized strain have the form

$$\frac{\partial \kappa_t}{\partial t}=\dot{\kappa}_t-\frac{\partial \kappa_t}{\partial s}\dot{s}=\boldsymbol{T}_{\kappa_t,q}\dot{\boldsymbol{q}}_s \quad ; \quad \frac{\partial^2 \kappa_t}{\partial t^2}=\boldsymbol{T}_{\kappa_t,q}\ddot{\boldsymbol{q}}_s+\boldsymbol{\alpha}_{\kappa_t,q} \tag{47}$$

$$\frac{\partial \kappa_b}{\partial t}=\dot{\kappa}_b-\frac{\partial \kappa_b}{\partial s}\dot{s}=\boldsymbol{T}_{\kappa_b,q}\dot{\boldsymbol{q}}_s \quad ; \quad \frac{\partial^2 \kappa_b}{\partial t^2}=\boldsymbol{T}_{\kappa_b,q}\ddot{\boldsymbol{q}}_s+\boldsymbol{\alpha}_{\kappa_b,q} \tag{48}$$

$$\frac{\partial \kappa_s}{\partial t}=\dot{\kappa}_s-\frac{\partial \kappa_s}{\partial s}\dot{s}=\boldsymbol{T}_{\kappa_s,q}\dot{\boldsymbol{q}}_s \quad ; \quad \frac{\partial^2 \kappa_s}{\partial t^2}=\boldsymbol{T}_{\kappa_s,q}\ddot{\boldsymbol{q}}_s+\boldsymbol{\alpha}_{\kappa_s,q} \tag{49}$$

$$\frac{\partial \varepsilon}{\partial t}=\dot{\varepsilon}-\frac{\partial \varepsilon}{\partial s}\dot{s}=\boldsymbol{T}_{\varepsilon,q}\dot{\boldsymbol{q}}_s \quad ; \quad \frac{\partial^2 \varepsilon}{\partial t^2}=\boldsymbol{T}_{\varepsilon,q}\ddot{\boldsymbol{q}}_s+\boldsymbol{\alpha}_{\varepsilon,q} \tag{50}$$

where $\alpha_{k,t}$, $\alpha_{k,b}$, $\alpha_{k,s}$, α_{ε} are the term in the acceleration that are independent of $\ddot{q}$.

When solving the dynamic equations of practical flexible multibody systems, the high-frequency oscillations of generalized strains lead to numerical difficulties. By applying model smoothing method and integrating-averaging the generalized strains, the high-frequency components can be filtered out. The generalized stresses after model smoothing can be expressed as

$$\bar{\boldsymbol{\sigma}}=\boldsymbol{\sigma}+\tfrac{1}{2}h\frac{\partial \boldsymbol{\sigma}}{\partial t}+\tfrac{1}{6}h^2\frac{\partial^2 \boldsymbol{\sigma}}{\partial t^2} \tag{51}$$

And the virtual power of deformation is written as

$$\delta w_e=\int_0^1 \delta(\frac{\partial \boldsymbol{\varepsilon}}{\partial t})^T\bar{\boldsymbol{\sigma}}d\xi \tag{52}$$

where, h is the smooth factor which can control the frequency remained in the system, and the generalized stresses can be obtained via eqs.(13)-(16). Combining with eqs.(13)-(16), (47)-(52), eq.(6) can be rewritten as

$$\delta w=(\delta\dot{\boldsymbol{q}})^T(\boldsymbol{M}\ddot{\boldsymbol{q}}+\boldsymbol{f}) \tag{53}$$

where, the generalized mass matrix and generalized force vector can be gathered as

$$\boldsymbol{M}=L_e\rho\int_0^1 \boldsymbol{T}_{\partial r_\xi,\partial t}^T\boldsymbol{T}_{\partial r_\xi,\partial t}d\xi \tag{54}$$

$$\begin{aligned}\boldsymbol{f}_q=L\int_0^1(&EI_t\kappa_t\boldsymbol{T}_{\kappa,t}^T+EI_b\kappa_b\boldsymbol{T}_{\kappa,b}^T\\&+GI_s\kappa_s\boldsymbol{T}_{\kappa,s}^T+EA\varepsilon\boldsymbol{T}_{\varepsilon,q}^T+\rho\boldsymbol{T}_{\partial r_\xi,\partial t}^T\boldsymbol{\alpha}_{\partial^2 r_\xi,\partial t^2})d\xi\end{aligned} \tag{55}$$

3.3 Constraint of the boom system

The boundary conditions for the boom system are defined as follows: the root joint at the outermost boom is rigidly fixed to the ground, while the node at the hydraulic cylinder remains constrained by the cylinder to maintain a fixed position. The external forces acting on the system include its self-weight and the load applied at the boom head.

Positional constraints are added between each boom section and its outer boom at the pin hole node, while positional constraints are added between each boom section and its inner boom at the boom head.

4 Modeling of pulley-rope system (PRS)

The PRS in a telescopic crane is illustrated in Fig.4. which is composed of a drum, several pulleys, ropes and hook. The rope is paid off from the drum, sequentially routed through the upper and lower pulleys, and ultimately anchored to a fixed point on the boom head.

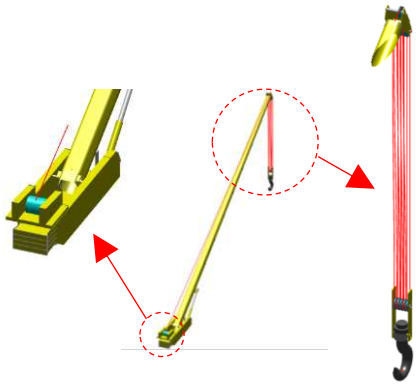


Fig.4 The pulley-rope system in cranes

In general, ropes are modeled as the flexible beam element with tiny section modulus, which can only withstand tension but not compression, while pulleys and hook are modeled as rigid bodies in PRS. The challenge of the modeling of PRS lies in the switch of the rope between pulleys and the rope in contact with pulleys, as a result of the dynamic contact between the rope and pulley. According to Sec.2, in order to simply describe the motion of the system and enable the division of elements more accurately, the contact points of pulley and rope are modeled as movable nodes in this section.

The axial strain of the rope ε_0 is assumed to be equal along the rope as the mass of the crane load is much larger than the mass of rope, and ε_0 is treated as the describe variables.

Based on different contact conditions, ropes can be categorized into two types: ropes in contact with

pulley and ropes between pulleys, where the ropes in contact with pulley can be modeled as a circular arc. For the ropes between pulleys, Hermite interpolation is applied to describe the shape of the rope.

4.1 Modeling of rope

According to Eq.(6), the virtual power of the rope is composed of the virtual power of inertial forces, the virtual power of external forces, and the virtual power of deformation.

The rope is divided into several segments by the movable nodes, and every segment is divided into several elements, as shown in Fig.5.

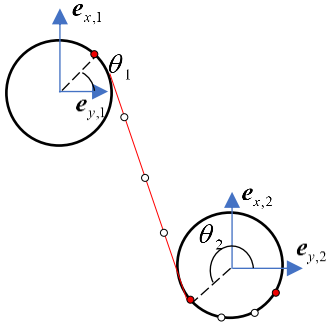


Fig.5 Discretization of rope element

The origin of a point on every rope segment can be obtained by interpolating the origins of its two endpoints. The normalized coordinates ξ is introduced to describe the shape of the rope. The positions of both endpoints of the rope can be described by the center location $\boldsymbol{r}_c$ and the azimuths of the rope. The azimuths of the start point and the end point of the rope and their derivatives with respect to arc length are denoted as (θ_1,θ_1') and (θ_2,θ_2'). γ is the rotation angle of the pulley, and L is the length of the rope. $\boldsymbol{e}_x$ and $\boldsymbol{e}_y$ are the base vectors of the coordinate system of the pulley. The arc length of the of the start point and the end point of the rope are denoted as s_1 and s_2, so the arc length of an arbitrary point on the rope can be expressed as

$$s=(1-\xi)s_1+\xi s_2 \tag{56}$$

The describe variables of every pulley can be gathered as

$$\boldsymbol{q}=[\gamma;\theta_1;s_1;\theta_2;s_2] \tag{57}$$

4.1.1 Rope in contact with pulley

As shown in Fig.5, the rope in contact with pulley conform to the contour of the pulley due to its negligible bending stiffness. The origin of an arbitrary point can be described by the azimuth angle θ.The derivatives with respect to arc length (θ') can obtained by Hermite interpolation

$$\theta=N_1\theta_1+N_2\theta_2+L(N_3\theta_1'+N_4\theta_2') \tag{58}$$

$$\theta'=L^{-1}(N_1'\theta_1+N_2'\theta_2+L(N_3'\theta_1'+N_4'\theta_2')) \tag{59}$$

The origin of an arbitrary point can be expressed as

$$\boldsymbol{r}_\xi=\boldsymbol{r}_c+r(\cos\theta\boldsymbol{e}_x+\sin\theta\boldsymbol{e}_y) \tag{60}$$

Take the derivatives with respect to arc length of Eq.(60), one can get

$$\boldsymbol{r}_\xi'=r(\cos\theta\boldsymbol{e}_y-\sin\theta\boldsymbol{e}_x)\theta' \tag{61}$$

The material velocity and acceleration of the origin can be expressed as

$$\frac{\partial\boldsymbol{r}_\xi}{\partial t}=\dot{\boldsymbol{r}}_\xi-\boldsymbol{r}_\xi'\dot{s}=\boldsymbol{T}_{\partial r,\partial t}\dot{\boldsymbol{q}} \tag{62}$$

$$\frac{\partial^2\boldsymbol{r}_\xi}{\partial t^2}=\boldsymbol{T}_{\partial r,\partial t}\ddot{\boldsymbol{q}}+\boldsymbol{\alpha}_{\partial r,\partial t} \tag{63}$$

4.1.2 Rope between pulleys

Given that the tensile force in the rope significantly exceeds its gravity, the rope between pulleys can be assumed to be a straight line, and the origin of arbitrary point can be obtained via Hermite interpolation.

$$\boldsymbol{r}_\xi=N_1\boldsymbol{r}_1+N_2\boldsymbol{r}_2+L(N_3\boldsymbol{r}_1'+N_4\boldsymbol{r}_2') \tag{64}$$

where, $\boldsymbol{r}_1$ and $\boldsymbol{r}_2$ are the origin of the end points of the rope between the pulleys, and they can be calculated according to Eq.(60). The derivatives with respect to arc length $\boldsymbol{r}_1'$ and $\boldsymbol{r}_2'$ can be approximated as

$$\boldsymbol{r}_i'=-(s_2-s_1)(1+\varepsilon_0)(\cos\theta_i\boldsymbol{e}_{y,i}-\sin\theta_i\boldsymbol{e}_{x,i}) \tag{65}$$

The material velocity and acceleration of the origin can be expressed as the same form as Eqs.(62)-(63).

4.1.3 Axial strain of rope

Considering the contact between the rope and the pulley, in order to approximate the variation in rope strain over the pulley, axial strain of an arbitrary point

of the rope can be obtained by the derivatives with respect to arc length of the its origin

$$\varepsilon_\xi = \left\| \boldsymbol{r}'_\xi \right\| - 1 \tag{66}$$

Axial strain is characterized by high-frequency, low-amplitude oscillations, which can significantly degrade the efficiency of dynamic simulations. Therefore, model smoothing method is employed, involving the integral averaging of the strain. The derivative of strain with respect to time and arc length can be expressed as

$$\dot{\varepsilon}_\xi = (1+\varepsilon_\xi)^{-1} (\boldsymbol{r}'_\xi)^T \dot{\boldsymbol{r}}'_\xi \tag{67}$$

$$\varepsilon'_\xi = (1+\varepsilon_\xi)^{-1} (\boldsymbol{r}'_\xi)^T \boldsymbol{r}''_\xi \tag{68}$$

$$\varepsilon''_\xi = (1+\varepsilon_\xi)^{-1} ((\boldsymbol{r}'_\xi)^T \boldsymbol{r}'''_\xi + (\boldsymbol{r}''_\xi)^T \boldsymbol{r}''_\xi) - (1+\varepsilon_\xi)^{-1} (\boldsymbol{r}'_\xi)^2 \tag{69}$$

The material velocity and acceleration of the axial strain can be expressed as

$$\partial \varepsilon_\xi / \partial t = \dot{\varepsilon}_\xi - \varepsilon'_\xi \dot{s} = \boldsymbol{T}_{\partial\varepsilon,\partial t} \dot{\boldsymbol{q}} \tag{70}$$

$$\begin{aligned} \partial^2 \varepsilon_\xi / \partial t^2 &= \ddot{\varepsilon}_\xi + \varepsilon''_\xi \dot{s}^2 - 2\dot{\varepsilon}'_\xi \dot{s} - \varepsilon'_\xi \ddot{s} \\ &= \boldsymbol{T}_{\partial\varepsilon,\partial t} \ddot{\boldsymbol{q}} + \boldsymbol{\alpha}_{\partial\varepsilon,\partial t} \end{aligned} \tag{71}$$

The axial strain after denoising can be written as

$$\bar{\varepsilon}_\xi = \varepsilon_\xi + \tfrac{1}{2} h (\partial \varepsilon_\xi / \partial t) + \tfrac{1}{6} h^2 (\partial \varepsilon_\xi^2 / \partial t^2) \tag{72}$$

where, h is the denoising factor.

4.2 Components of PRS in a crane

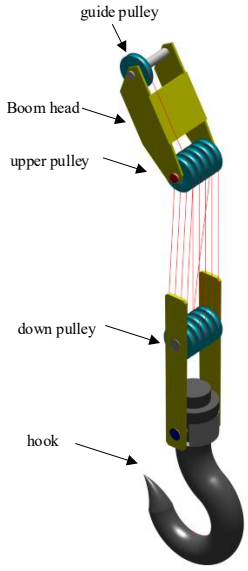


Fig.6 Components of PRS in a crane

4.2.1 Drum

The drum serves as the start point of the rope. Given that the azimuth angle at the rope exit point is θ_d, and its arc length coordinate is s_d, then the origin of the start point of the first segment of rope, can be obtained

$$\boldsymbol{r}_d = \boldsymbol{r}_{d,0} + r_d (\cos\theta_d \boldsymbol{e}_{x,d} + \sin\theta_d \boldsymbol{e}_{y,d}) \tag{73}$$

where, the origin of the drum $\boldsymbol{r}_{d,0}$, which lies at the center of the cross section of the drum, and the radius of the drum is r_d, the base vector of the coordinate system of the drum are $\boldsymbol{e}_{x,d}$ and $\boldsymbol{e}_{y,d}$. The describe variables of the drum can be gathered as

$$\boldsymbol{q} = [s_d; \theta_d] \tag{74}$$

4.2.2 Hook

The origin of the local coordinate system of the hook lies at the center of the axis of the down pulleys, and we can assume that it is located directly below $\boldsymbol{r}_{up,c}$, the center of the top pulley shaft. The origin of the local coordinate system is determined by the distance between the axis of upper pulleys and down pulleys (h_z), and the rotations can be determined by the cardan angles of the hook (α_h, β_h, γ_h). The position vector of the centroid of the hook can be expressed as

$$\boldsymbol{r}_{c,h} = \boldsymbol{r}_{up,c} - h_z \boldsymbol{g}_z + \boldsymbol{R}_h \boldsymbol{r}_{c_0,h} \tag{75}$$

where, $\boldsymbol{R}_h$ is the rotation matrix generated by (α_h, β_h, γ_h), and $\boldsymbol{r}_{c_0,h}$ is the position vector from the origin to the centroid in the local coordinate system of hook. The describe variables of the hook can be gathered as

$$\boldsymbol{q} = [h_z, \alpha_h, \beta_h, \gamma_h] \tag{76}$$

4.2.3 Pulleys

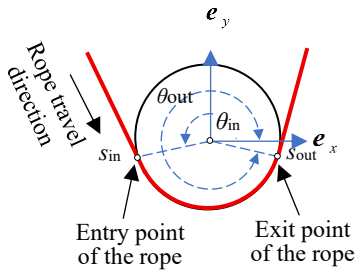


Fig.7 The description of rope on pulley

The pulleys are categorized into upper pulleys and

down pulleys, the difference of which lies in their bases. The base body of the upper pulley is the boom head, and the origin of the center of upper pulley is $\boldsymbol{r}_{c,up}$. The base body of the down pulley is hook, and the origin of the center of down pulley is $\boldsymbol{r}_{c,dp}$. They can be expressed as

$$\boldsymbol{r}_{c,up} = \boldsymbol{r}_{0,b} + \boldsymbol{R}_b \boldsymbol{r}_{0,up} \tag{77}$$

$$\boldsymbol{r}_{c,dp} = \boldsymbol{r}_{0,h} + \boldsymbol{R}_h \boldsymbol{r}_{0,down} \tag{78}$$

where, $\boldsymbol{r}_{0,b}$ and $\boldsymbol{R}_b$ are the origin and rotation matrix of the boom head, while $\boldsymbol{r}_{0,h}$ and $\boldsymbol{R}_h$ are the origin and rotation matrix of the hook. $\boldsymbol{r}_{0,up}$ and $\boldsymbol{r}_{0,down}$ are the origin of the pulley center in the boom head coordinate system and hook coordinate system, which are constants. Then the origin of the pulley center can be obtained. Take time derivatives of Eqs.(77)-(78), one can obtain that

$$\dot{\boldsymbol{r}}_{c,up} = \dot{\boldsymbol{r}}_{0,b} + \boldsymbol{\omega}_b \times \boldsymbol{r}_{0,up} \tag{79}$$

$$\dot{\boldsymbol{r}}_{c,dp} = \dot{\boldsymbol{r}}_{0,h} + \boldsymbol{\omega}_h \times \boldsymbol{r}_{0,down} \tag{80}$$

where, $\dot{\boldsymbol{r}}_{0,b}$ and $\boldsymbol{\omega}_b$ are the velocity and angular velocity of the boom head, while $\boldsymbol{r}_{0,h}$ and $\boldsymbol{\omega}_h$ are the velocity and angular velocity of the hook.

The motion of pulleys can be decomposed into the displacement of the center of pulley and the rotation around its axis, and the former motion can be considered to follow the movement of the boom.

4.3 Virtual power of the PRS

The inertial virtual power of the rope can be expressed as

$$\delta w_r = \rho(s_5 - s_1)\int_0^1 \delta\left(\frac{\partial \boldsymbol{r}_\xi}{\partial t}\right)^T \left(\frac{\partial^2 \boldsymbol{r}_\xi}{\partial t^2}\right) d\xi = (\delta \dot{\boldsymbol{q}})^T (\boldsymbol{M}_r \ddot{\boldsymbol{q}} + \boldsymbol{f}_r) \tag{81}$$

The deformation virtual power of the rope can be expressed as

$$\delta w_e = EA(s_2 - s_1)\int_0^1 (\delta\dot{\varepsilon})^T \bar{\varepsilon}_\xi d\xi = (\delta \dot{\boldsymbol{q}})^T \boldsymbol{f}_e \tag{82}$$

The inertial virtual power of the hook can be expressed as

$$\begin{aligned}\delta w_h &= m_h(\delta \dot{\boldsymbol{r}}_{c,h})^T(\ddot{\boldsymbol{r}}_{c,h} - \boldsymbol{g}) + (\delta\boldsymbol{\omega}_h)^T(\boldsymbol{J}\cdot\dot{\boldsymbol{\omega}}_h + \boldsymbol{\omega}_h \times \boldsymbol{J}_h \cdot \boldsymbol{\omega}_h) \\ &= (\delta \dot{\boldsymbol{q}})^T (\boldsymbol{M}_h \ddot{\boldsymbol{q}} + \boldsymbol{f}_h)\end{aligned} \tag{83}$$

The inertial virtual of the rotation of the pulley can be expressed as

$$\delta w_p = (\delta\dot{\gamma})^T J_p \boldsymbol{e}_{z,i} \ddot{\gamma} = (\delta \dot{\boldsymbol{q}})^T (\boldsymbol{M}_\gamma \ddot{\boldsymbol{q}} + \boldsymbol{f}_\gamma) \tag{84}$$

By summing up the above terms, the virtual power equation of the system can be obtained, which has the same form as Eq.(6).

4.4 Constraint of the PRS

4.4.1 Constraint of material velocity of the pulley

The contact point can be treated as a point both on rope and on pulley. Since the no-sliding contact between pulley and rope, the results of material velocity of the boundary point of each segment of the rope should be consistent, no matter it is treated as a point on rope or on pulley.

As shown in Fig.7, the material velocity of the contact point on the rope ($\boldsymbol{r}_r$) can be obtained according to Eq.(3).

$$\begin{aligned}\partial \boldsymbol{r}_r / \partial t = {} & \dot{\boldsymbol{r}}_c - (\tilde{\boldsymbol{r}}_r - \tilde{\boldsymbol{r}}_c)\boldsymbol{\omega} \\ & + r(\cos\theta \boldsymbol{e}_y - \sin\theta \boldsymbol{e}_x)(\dot{\theta} - (s_{out} - s_{in})^{-1}\theta' \dot{s})\end{aligned} \tag{85}$$

while the material velocity the contact point on the pulley ($\boldsymbol{r}_p$) has the form

$$\partial \boldsymbol{r}_p / \partial t = \dot{\boldsymbol{r}}_c - (\tilde{\boldsymbol{r}}_p - \tilde{\boldsymbol{r}}_c)\boldsymbol{\omega} + r\dot{\gamma}\boldsymbol{e}_z \times (\cos\theta \boldsymbol{e}_x + \sin\theta \boldsymbol{e}_y) \tag{86}$$

Comparing Eqs.(85)-(86), the two material velocities are equal in the tangential direction, which can be rewritten as a constraint on the rotation angle of the pulley

$$\dot{\gamma} = r^{-1}(\dot{\theta} - (s_{out} - s_{in})^{-1}\theta' \dot{s}) \tag{87}$$

Eqs.(87) indicates that the constraint only restricts the change rate of the describe variables, which is a non-holonomic constraint.

4.4.2 Constraint of the drum

The motion of the rope on the drum comprises two components: the rotation of the drum itself and the winding of the rope relative to the grooves. The rotation of the drum constitutes the convected motion, while the winding of the rope onto the grooves represents the relative motion.

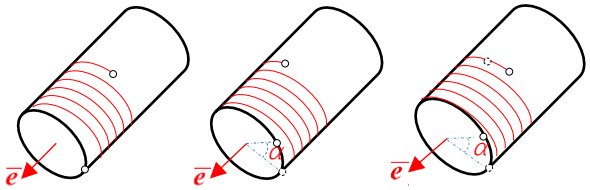


Fig.8 The motion decompositon of the drum

The influence of deformation of the boom on the rope alignment from the drum to the guide pulley is neglected, so the resulting absolute motion of the exit point of the rope on the drum is the displacement along the drum. As a result, the relationship between α, the rotation angle of the drum, and θ_d, the azimuth angle at the rope exit point, can be concluded as

$$\alpha = -\theta_d \tag{88}$$

And the arc length of the exit point can be expressed as

$$s_d = -(1+\varepsilon_0)^{-1}\kappa\alpha \tag{89}$$

where, κ represents pitch of the drum groove. Eqs.(88) -(89) establish the relationship between drum rotation and motion of the rope and pulleys.

5 Dynamics of telescopic boom crane with pulley-rope system

Characterized as a large-scale multibody system, crane is composed of a telescopic boom system and a set of PRS, as illustrated in Fig.4.

Due to the coupled nature of the boom and the pulley-rope system, the crane exhibits complex dynamic behavior when hoisting and lowering heavy loads. Taking an example of a truck crane with eight-section telescopic boom, the dynamics of the crane system under hoisting loads is analyzed this paper.

The main parameters of the crane system are listed in Tab.1.

Tab.1 Main parameters of the crane system

Parameter	Value
Boom length(m)	53
Working angle(°)	30
Elastic modulus of the boom(N)	2e7
Density of the boom(kg/m^3)	7850
Density of the rope(kg/m)	0.5
Elastic modulus of the rope(N)	8e6
Reeving ratio	10

The initial system configuration is defined as the state under no external load. The initial values for the dynamic analysis are assigned based on the static solution obtained after applying the load and gravity.

5.1 The number of turns of the drum

The drum's number of turns is controlled such that the hoisted load reaches the ground precisely when the drum stops. A polynomial interpolation function is adopted to ensure the second-order continuity of the drum rotation angle, thereby enabling smooth dynamics computations. The number of turns of the drum is illustrated in Fig.9.

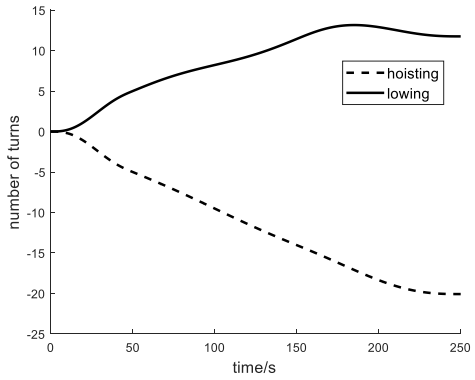


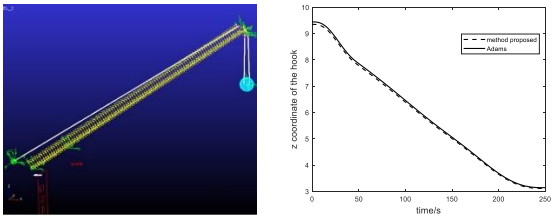
Fig.9 The cross-section of the boom

When the load is being lifted, it is first raised to a height slightly above the specified level, at which point the hoisting velocity drops to zero, followed by a gradual lowering process to reduce impact.

By specifying the number of turns of the drum, the dynamic processes of hoisting and lowering different loads are simulated.

5.2 Verification of the proposed method

To verify the correctness of the method proposed in this paper, a model of the pulley-rope system was established in ADAMS for comparison in which the boom system is set as rigid body. As shown in Fig.10 (a), and the results are shown in Fig.10(b). Through the simulation of drum rotation using a winch model, the relevant parameters correspond to the drum speed consistent with the aforementioned example.



(a)Model in ADAMS (b) comparison of results

Fig.10 The comparison of the proposed method and ADAMS

The variation in the vertical component of the hook with time is illustrated in Fig.10(b). The comparative analysis indicates that the results of this study align with those obtained from ADAMS in terms of trends, particularly in the vertical displacement of the hook, which shows near consistency. While ADAMS neglects rope deformation and fails to characterize the oscillation of the system during hoisting, the simulation results of this study better capture the actual dynamic behavior.

5.3 Simulation results of the load lowering process

5.3.1 Displacement of the boom head

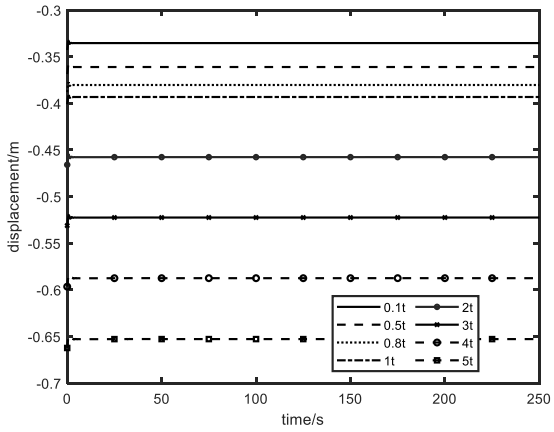


Fig.11 Displacement of the boom head varying with time

The displacements of the boom head are illustrated in Fig.11. We can find that, the greater the lifting load is, the larger the displacement of the boom head will be. The slight oscillation of the boom head at the initial moment is attributed to the impulse exerted on the system during its transition from a stationary state to motion. The displacement of the boom head remains largely unchanged during the motion of the lifting load.

5.3.2 Position of the hook when lowering

The positions of the hook under different loads are analyzed in this section, which is shown in Fig.12.

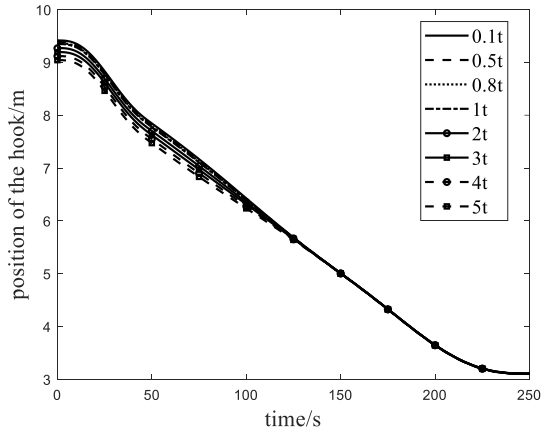


Fig.12 z coordinate of the hook varying with time when lowing

From Fig.12, the components in the direction of gravity vary with the lifting load, but the difference between them diminishes over time and eventually vanishes. The main cause of the difference at the initial time lies at the displacement of the boom head under different lifting loads. The greater the mass of the lifting load, the larger the displacement of the boom head is, with the initial position of hook being lower.

5.3.3 Changes laws of the PRS when lowering

The rotation angles of the pulleys under different loads are illustrated in Fig.13.

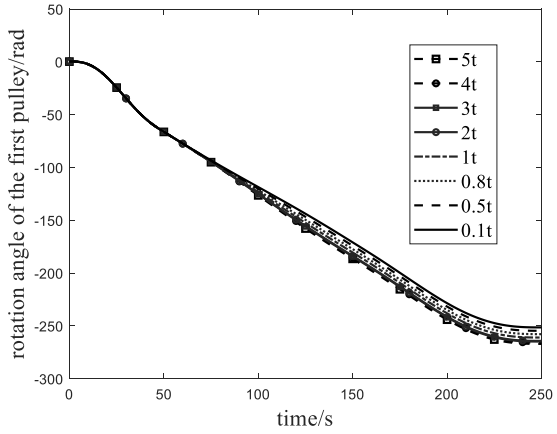


Fig.13 Rotation angle of the first pulley varying with time when lowing

Given the assumption of no-sliding contact between pulley and rope, the variation pattern of the pulley's rotation angle is the same as that of the drum's rotation angle.

The arc lengths of the enter point of guide pulley

under different loads are illustrated in Fig.14.

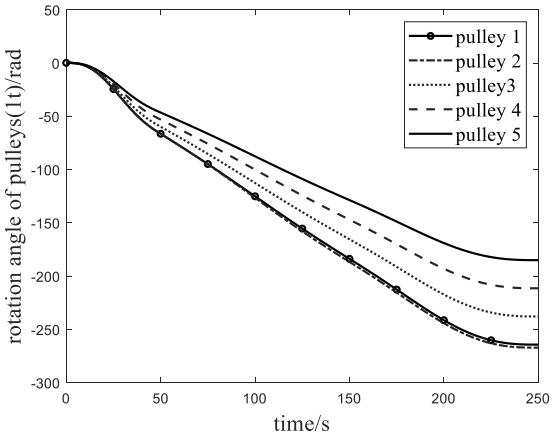


Fig.14 Rotation angle of the pulleys varying with time when lowing

Since the load is being lowered and the drum is unwinding rope, the length of the rope in the system increases, while the arc length coordinate at each point on the pulley should be decreasing. The variation pattern of the pulley's arc length is the same as that of the drum's rotation angle.

The arc lengths of the enter point of pulley numbered from 1 to 5 under the same loads are illustrated in Fig.15.

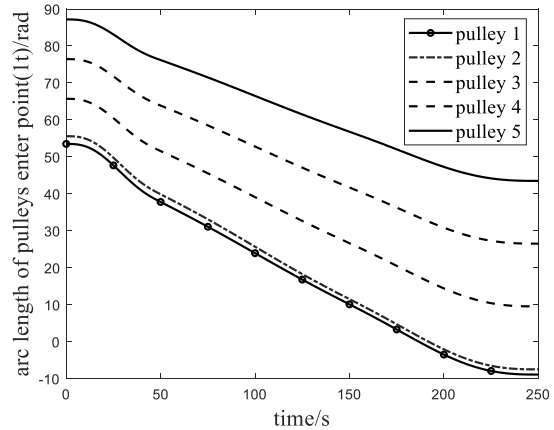


Fig.15 Arc length of the pulleys varying with time when lowing

From Fig.15, we can find that the variation patterns of the arc length for each pulley are fundamentally identical.

5.3.4 Displacement of the hook when hoisting

Through Fig.16, the displacement variation of the boom head during load hoisting is largely identical to that during load lowering, as the position of the boom head remains largely unchanged throughout both processes.

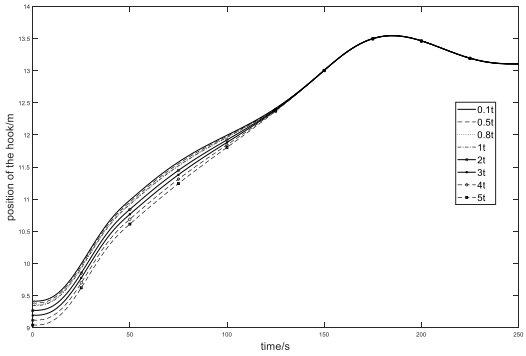


Fig.16 z coordinate of the hook varying with time when hoisting

5.3.5 Changes laws of the PRS when hoisting

The rotation angles of the pulleys under different loads are illustrated in Fig.17.

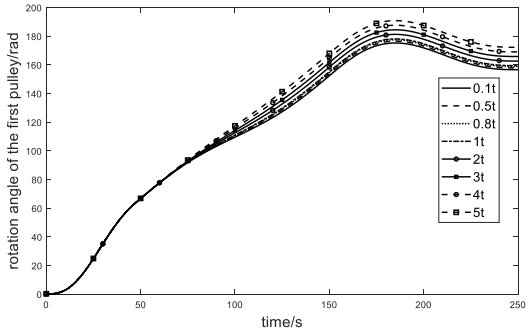


Fig.17 rotation angles of the pulleys varying with time when hoisting

The rotation angle of pulleys numbered from 1 to 5 are drawn in Fig.18, and the rotation angle of the pulley which is closer to the anchor is smaller.

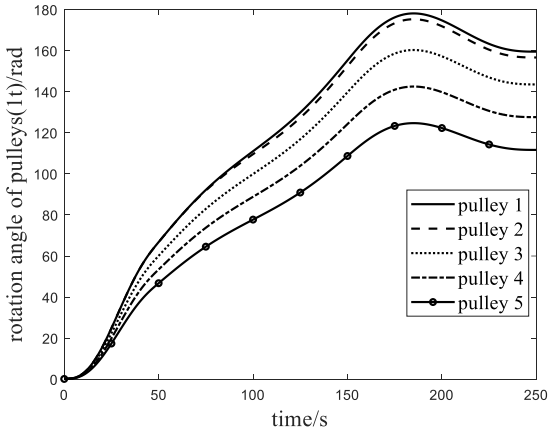


Fig.18 rotation angles of the pulleys varying with time when hoisting

The arc lengths of the enter point of pulleys numbered from 1 to 5 are drawn in Fig.19, and the arc length of the pulley which is closer to the anchor is smaller. It can be observed that the variation patterns of the rotational angle and arc length coordinates during the lowering and hoisting processes coordinate with the rotation of the drum.

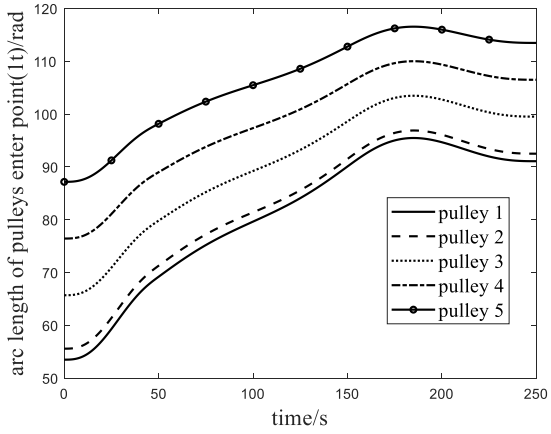


Fig.19 Arc length of the pulleys varying with time when hoisting

5.4 High-frequency oscillations of the system

During the dynamic analysis, in addition to the high-frequency oscillations observed in the rope strain, the azimuth angle of the pulley also exhibits high-frequency, low-amplitude oscillations. As shown in the Fig.20, oscillations do not represent the true physical behavior of the system, and dramatically reduce efficiency of solution. Due to the minimal variation in the azimuth angle, constraints are applied to it in order to mitigate the adverse effects of high-frequency oscillations on the computational efficiency of the system solution.

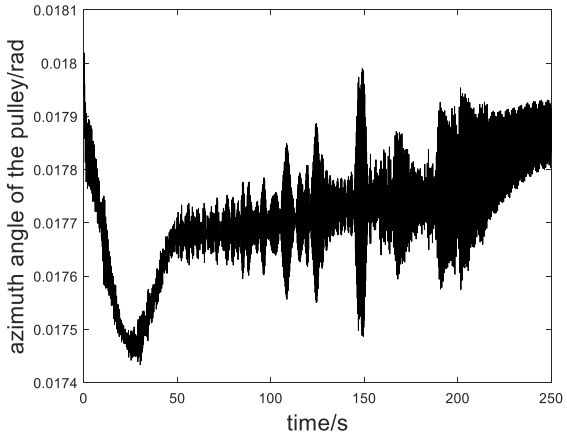


Fig.20 azimuth angle of the pulleys before smoothing varying with time

After applying the constraints, the computational time required to solve the dynamic equations was reduced from 10 hours to 40 minutes, and the number of time steps was reduced from 38,000 to 3,000.

6 Conclusion

For a multibody system such as crane, which consists of boom and pulley-rope system, large deformations occur under heavy loads, and the relative motions between components exhibit dynamic boundary characteristics. In this paper, axial strain and curvature of the cross-sectional are adopted as generalized strains to describe the deformation of geometry nonlinear beam elements. The contact points between pulleys and ropes are modeled as movable nodes under spatial description, which serve as the end point of the rope elements. To address the issue of low computational efficiency in solving the dynamic equations, a model smoothing method is applied to accelerate the solution process. Numerical examples demonstrate that the proposed method effectively captures the dynamic response of the crane system and validates the accuracy and practicality of the movable node elements. This approach can provide a reliable reference for the dynamic analysis and engineering

application of multibody systems with moving loads or moving boundaries.

Subsequent research can conduct a dynamic analysis of the hoisted load during its contact process with the ground.

Reference

[1] Cha J.H., Roh M., Lee K.Y.: Dynamic response simulation of a heavy cargo suspended by a floating crane based on multibody system dynamics. Ocean. Eng. 37, 1273-1291 (2010)

[2] Radomir M.: Modelling the dynamic behavior of the truck-crane. Transport. 26(4): 410-417 (2011)

[3] Namkug K., Ha S.: Dynamic response analysis of heavy load lifting operation in shipyard using multi-cranes. Ocean. Eng. 83, 63-75 (2014)

[4] Bin H., Tang W., Cao J.: Virtual prototyping-based multibody systems dynamics analysis of offshore crane. Int. J. Adv. Manuf. Technol. 75, 161-180 (2014)

[5] Qi Z., Li S., Zhang A.M.: A nonlocal nonlinear stiffened shell theory with stiffeners modeled as geometrically-exact beams. Comput. Methods Appl. Mech. Rngrg. 397,115150 (2022)

[6] Prakash R. S., Barik M.: Dynamic response of stiffened bridge decks subjected to moving loads. J. Vib. Eng. Technol. 9(8), 1983-1999 (2021)

[7] Wang C., Zhen B.: The study for the influence of nonlinear foundation on responses of a beam to a moving load based on volterra integral equations[J]. J. Vib. Eng. Technol. 9(5): 939-956 (2021)

[8] Mahdi S., Akbarzadeh A.: A constrained assumed modes method for solution of a new dynamic equation for an axially moving beam. Comput. Math. Appl. 72, 2167-2180 (2016)

[9] Al-Bedoor B.O., Khulief Y.A.: An approximate solution of beam vibrations during axial motion. J. Sound Vib. 192(1), 159-171 (1996)

[10] Nikhil S., Sharma I., Gupta S.S. Dynamics of variable length geometrically exact beams in three-dimensions. Int. J. Solids Struct. 191-192,614-627 (2020)

[11] Carlo S., Nguyen T.L., Hjiaj M.: An energy-momentum method for in-plane geometrically exact Euler-Bernoulli beam dynamics. Int. J. Numer. Meth. Engng. 102(2), 99-134 (2015)

[12] Tang J.L., Ren G.X., Zhu W.D., Ren H.: Dynamics of variable-length tethers with application to tethered satellite deployment. Commun. Nonlinear Sci. Numer. Simul. 16, 3411-3424 (2011)

[13] Vahid S., Mirdamadi H.R., Ghayour M, et al. Spectral finite element for vibration analysis of cracked viscoelastic Euler-Bernoulli beam subjected to moving load. Acta Mech. 226, 4259-4280 (2015)

[14] F Ju, Choo Y-S. Super element approach to cable passing through multiple pulleys. Int. J. Solids Struct. 42, 3533-3547 (2005)

[15] Chen Z., Yao B.: Modeling and Analysis of a Cable-pulley Actuated Lifting System. IFAC-PapersOnLine. 55-37, 320-325 (2022)

[16] Yun P., Wei Y., Zhou M.: Efficient modeling of cable-pulley system with friction based on arbitrary-Lagrangian-Eulerian approach. Appl. Math. Mech. - Engl. Ed. 38(12), 1785-1802 (2017)

[17] Ainhoa G., Aginagalde A., Tato W., et al.: Impact of surface roughness on the coefficient of friction of polymer-on-polymer contacts for deflection pulley-rope systems in the lift industry. Friction. 12(9), 2126-2138 (2024)

[18] Li C., Wang D., Sun Y., et al.: Bending fatigue damage behavior of wire rope in hoisting system of drilling rig. Tribol. Int. 187, 108745 (2023)

[19] Chang X., Chen X., Dong Y., et al: Friction and wear behavior between crane wire rope and pulley under different contact loads. Lubricants. 10, 337 (2022)

[20] Liz R., Kubota Y., Venture G., et al: Inverse dynamic control via “simulation of feedback control” by artificial neural networks for a crane system. Control Eng. Pract. 94, 104203 (2020)

[21] Jin X.J., Jung J., Piao J., et al.: Solving the pulley inclusion problem for a cable-driven parallel robotic system: Extended kinematics and twin-pulley mechanism. J. Mech. Sci. Technol. 32(6), 2829-2838 (2018)

[22] Radek B., Hajžman M., Polach P.: Nonlinear dynamics of a cable-pulley system using the absolute nodal coordinate formulation. Mech. Res. Commun. 82, 21-28 (2017).

[23] Xue R., Ren B., Yan Z., et al.: A cable-pulley system modeling based position compensation control for a laparoscope surgical robot. Mech. Mach. Theory. 118, 283-299 (2017)

[24] Zhang X.G., Qi Z.H., Wang G., et al.: Model smoothing method of contact-impact dynamics in flexible multibody systems. Mech. Mach. Theory. 138, 124-148 (2019)

[25] Zhuo Y.P., Qi Z.H., Xu J.S.: A Dynamic Geometrical Nonlinear Slender Beam Element with Movable Nodes. J. Vib. Eng. Technol. 11, 3653-3675 (2023)